Double differential cross sections for neutron emission induced by 256 MeV and 800 MeV protons

S. Stamer and W. Scobel
I. Institut für Experimentalphysik, Universität Hamburg, Hamburg, Germany

W. B. Amian, R. C. Byrd, R. C. Haight, and J. L. Ullmann
Los Alamos National Laboratory, Los Alamos, New Mexico 87545

R. W. Bauer, M. Blann, and B. A. Pohl
Lawrence Livermore National Laboratory, Livermore, California 94550

J. Bisplinghoff
Institut für Strahlen- und Kernphysik, Universität Bonn, Bonn, Germany

R. Bonetti
Istituto di Fisica Generale Applicata dell'Università di Milano and Istituto Nazionale di Fisica Nucleare, Sezione di Milano, Milano, Italy
(Received 2 November 1992)

Double differential cross sections were measured for neutron emission induced by 256 MeV and 800 MeV protons incident on Li, Al, Zr, and Pb targets. The experimental spectra obtained are almost exclusively attributable to a preequilibrium emission mechanism and are compared to predictions made by several preequilibrium reaction models. The intranuclear cascade model reproduces the data quite well at both incident energies. Other approaches—the statistical multistep direct model and the hybrid model—reach the limit of applicability in their present form as the pion production threshold is crossed.
PACS number(s): 24.60.Gv, 25.40.−h

I. INTRODUCTION

Medium and intermediate energy reactions have been interpreted for some decades in terms of semiclassical reaction models, i.e., the intranuclear cascade [1, 2] and precompound models [3, 4]. During the past decade, increasing consideration has been given to quantum statistical approaches [5–7].

The theory of Feshbach, Kerman, and Koonin (FKK) [5] has been shown to give a reasonable interpretation of double differential cross sections in the continuum for incident energies of a few tens of MeV to 160–200 MeV [8–12]. The theory treats statistical multistep nucleon-scattering processes mediated via two-body N-N interactions, with the strength of the effective nucleon-nucleon interactions. The scattering processes are expressed by distorted wave Born approximation (DWBA) matrix elements.

The effective interaction in the application of FKK theory is described by a Yukawa potential with a range $r_0 = 1$ fm. It was found that its strength V_0, if treated as free parameter, decreases with increasing projectile energy to an extent that is expected if the (N, N) reaction probes the central scalar-isoscalar part of the effective NN interaction [9]. The increasing importance of higher-step contributions in statistical multistep direct emission (SMDE) is visible (1) in their contributions to backward angle cross sections and to low ejectile energies and (2) in the energy scaling $V_0(E_p)$, which is less pronounced than, e.g., that of the real part of optical model potentials [9, 11].

With the central part of the effective NN potential having a broad minimum around $E_p = 300$ MeV [13], we expect V_0 to decrease further as E_p approaches this value. At present, however, the applicability of the FKK model is restricted to projectile energies E_p not involving pionic degrees of freedom and to residual excitation energies below some 100 MeV, where the exciton particle may be reasonably described using quasibound wave functions. This is the motivation for the selection of $E_p = 256$ MeV in this work.

At substantially higher projectile energies, intranuclear cascade models (INC) with various degrees of sophistication [1, 2] have been successfully applied to the interpretation of reaction data [14, 15]. They are adequate for a description of the major fraction of the reaction cross section; the models should, however, also be tested for backward angle data to ensure that the semiclassical picture of an intranuclear cascade is physically reasonable and complete. There is some evidence that the INC model works well for the spectral pre-equilibrium continuum observed for $E_p = 585$ MeV [15]. It is clear that neutron spectroscopy at backward angles requires particular attention to be paid to background minimization if

the data are intended for a quantitative analysis.

In order to explore the INC model in the intermediate energy range $E_p < 1000$ MeV, we shall apply it in the HETC-KFAII [15, 16] version to data taken at 800 and 256 MeV with particular attention to background treatment, energy resolution, and statistics. Target mass numbers are expected to play a minor role, therefore the study is restricted to Zr, Pb, Al, and ^{7}Li (for determination of the neutron detector efficiency). Finally, the data will be used to test the semiclassical hybrid model [3] in a relativistic version of the code ALICE [17].

Experimental (p, xn) data suitable for a test of the reaction models mentioned have to extend over a broad spectral and angular range. Such data are available primarily for applied science [14, 15, 18] and often lack a careful treatment of background. In the present work, emphasis was put on these experimental aspects, too.

The paper is organized as follows. In Sec. II we describe the experimental setup. Section III is devoted to the data reduction with respect to background contributions and absolute cross section values, as well as to discussion of the qualitative features of the double differential cross sections. The discussion in Sec. IV focuses on a comparison of our data with the INC model, the FKK multistep model, and the hybrid preequilibrium model. Results are summarized in Sec. V.

II. EXPERIMENTAL PROCEDURE

The experiment was performed at the WNR facility of the Los Alamos Meson Physics Facility (LAMPF), which allows time structure of the beam to be matched to the requirements of neutron time-of-flight measurements. The time structure chosen consisted of "micropulses" spaced 5.7 μs from one another and grouped into "macropulses" of some 700 μs duration and 12 Hz or 40 Hz recurrence (at 256 and 800 MeV, respectively). The micropulses contained some $(2-3) \times 10^8$ protons each, which affords a mean proton beam intensity of 40 and 250 nA, respectively. This intensity comes at the price, however, of having so large a number of valid events concentrated in so short a time span that it is impractical to record them event by event. Instead, time-of-flight spectra were accumulated in CAMAC histogramming memory modules, then transferred to the data acquisition computer and saved on tape every 12 min.

The target and detector configuration used is shown in Fig. 1. The target position was centered in a low mass area with massive construction materials being at least 5 m away. Targets were metallic foils of $70-150$ mg/cm^2 thickness mounted in frames with typically 25.4 mm inner diameter. They were located in a thin walled scattering chamber [19]. A secondary electron monitor (SEM) was used to measure the number of protons per macropulse of beam. It was calibrated by irradiating Al foils and recording the residual activity produced by the ^{27}Al$(p, 3pn)^{24}$Na, ^{27}Al$(p, x)^{22}$Na, and ^{27}Al$(p, x)^7$Be reactions [20, 21]. An inductive pick-off provided the time reference for time-of-flight (TOF) measurements, indicating the arrival of each microburst.

The 5 neutron TOF paths at laboratory angles

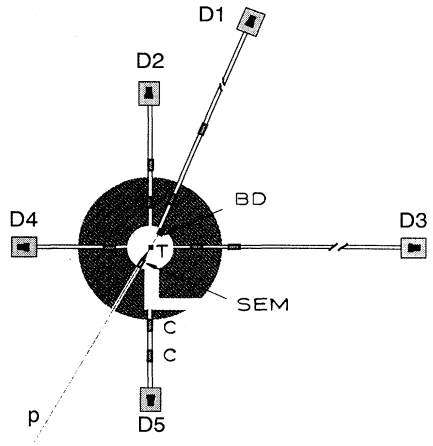

FIG. 1. Schematic diagram showing location of target (T), detectors (D1–D5), beam dump (BD), collimators (C), and secondary electron monitor/time pick-off (SEM).

$7.5°, 30°, 60°, 120°$, and 150° consisted of cylindrical tubes of roughly 75 cm diam partly running below ground level. All 5 paths were equipped with two sets of collimators (see Fig. 1) to minimize the number of inscattered neutrons. Their clearance assured that all neutrons coming from the targets would be seen by the neutron detectors. The detectors used were cylindrical liquid scintillators. All detectors had been used before in neutron TOF spectroscopy such that their characteristics were well known [8, 22, 23]. Table I gives a summary of their features. The different dimensions were selected in an attempt to compensate, in combination with the varying paths lengths, for the substantial decrease of the counting rates from forward to backward angles. Scintillator cells and light guides (partly) had a reflective coating of TiO_2.

The overall time resolutions listed in Table I are poorer at 256 MeV (Δt_{256}) than at 800 MeV (Δt_{800}), because the lower energy was provided by letting the protons drift the last two-thirds of the accelerator section. They correspond to energy resolutions $\Delta E_n(\Delta t)$ for the (p, n_0) transitions that are given in Table I. Each detector had a "veto paddle" in front of it, a thin (6 mm) plastic scintillator to suppress signals produced by elastically scattered protons and other charged particles that were not yet removed by the magnetic sweep dipoles (B=0.1 T) at the beginning of the flight paths (Fig. 1). Multiplier gains were monitored throughout the experiment by means of weak radioactive sources (Th, $E_\gamma = 2.6$ MeV from ^{208}Tl).

Particular care was taken in setting pulse height thresholds according to several criteria: First, low energy neutrons and γ rays were to be suppressed for count rate reasons. Second, the Compton edges of 2.6 MeV γ rays from the sources were to be recorded between macropulses in order to monitor multiplier gains. Finally, as data were not being taken event by event, thus precluding off-line adjustment of thresholds, two different thresholds were to be used as a safety measure and as a means to verify detection efficiency calculations (see

TABLE I. Neutron detector data.

Detector no.	1	2	3	4	5
Diam. × thickn. (cm)	25.4 × 5.1	10.2 × 10.2	30.5 × 20.3	25.4 × 5.1	30.5 × 20.3
Material[a]	BC501	NE213	BC501	BC501	BC501
TOF path (m)	50.36	29.76	58.61	23.34	30.99
Angle Θ_{lab} (deg)	7.5	30.0	60.0	120.0	150.0
Solid angle (μ sr)	20.0	9.23	21.3	93.0	76.1
Δt_{256} (ns)	5.8	3.5	6.5	4.9	5.9
$\Delta E_n(\Delta t_{256})$ (MeV)	16	16	15	29	26
Δt_{800} (ns)	1.1	1.0	2.7	3.6	2.1
$\Delta E_n(\Delta t_{800})$ (MeV)	22	36	49	164	72
E_n^{th} (MeV_{pe}) monitor	2.8	2.8	2.3	2.8	2.5
Low[b]	11.5	11.0	10.4	9.4 (24)	10.6 (21)
High[b]	23	24	21	24 (48)	21 (38)
$\eta_0(E_n > 300$ MeV)[c]	2.23%	4.8%	12.0%	1.47%	12.9%

[a]H/C ratios used are 1.213 for NE213 and 1.287 for BC501.
[b]Values in parentheses refer to $E_p = 800$ MeV runs only.
[c]η_0 refers to low threshold.

Sec. III). This required a total of three thresholds for each neutron detector, a very low ("monitor") one to record the amplitude of the source γ signals and two more ("low" and "high") to select neutron signals for time-of-flight measurements. The thresholds were set using the Compton edges of ^{22}Na and ^{88}Y sources, and they are listed in Table I in proton equivalent MeV [24]. Due to the height of the "low" and "high" thresholds, electronic n-γ pulse shape discrimination was superfluous. The logic was wired so that (i) scintillator signals passing the "monitor" (but not the "low") threshold were amplitude analyzed only *between* beam macropulses and (ii) scintillator signals passing the "low" (but not the "high") threshold and those passing the "high" threshold were separately time-of-flight analyzed only *during* beam macropulses.

Signal processing electronics and data acquisition were much as described in Ref. [25]. A number of scalers were set up to monitor consistency of count rates and to check dead times.

III. EXPERIMENTAL RESULTS AND DATA REDUCTION

A. Experimental procedure

With the setup described above, data were taken over a period of 10 days with beam on target during more than 80% of the time. Due to the histogramming memories used, dead times could be generally kept below 5% and statistics accumulated to permit measurement of differential cross sections over 5 orders of magnitude. Each run was supplemented by a background run with steel cylinder shadow bars of 10 cm diam and 45 cm length being inserted at 2–3 m distance from the target into the TOF paths. Two representative TOF spectra are shown in Fig. 2. The γ peaks were used for determination of the absolute time scale and time resolution (Table I). The background spectra normalized to the same (Ugr) secondary electron monitor count rate represent an integral correction of the order of 1% of the effect under study (Eff.).

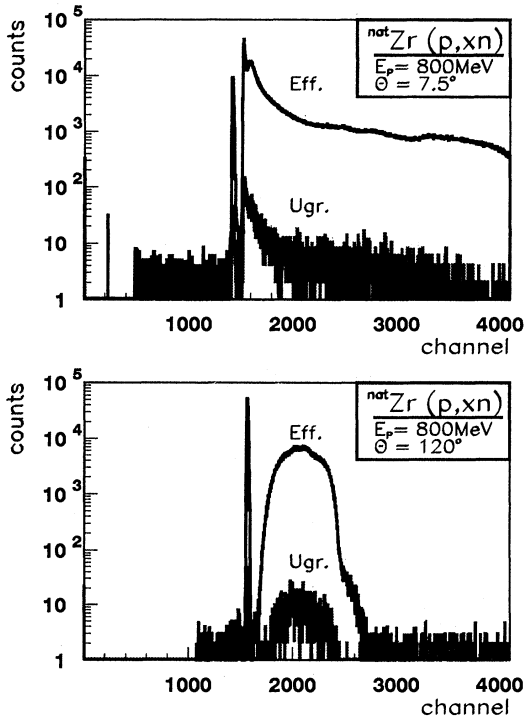

FIG. 2. Examples of neutron TOF spectra (Eff.) and background spectra (Ugr) at angles of 7.5° and 120°, for ^{nat}Zr targets.

The neutron TOF spectra were converted into energy spectra and transformed into double differential cross sections in the center-of-mass system with the efficiencies $\eta(E_n^{\rm th}, E_n)$ calculated for the threshold values $E_n^{\rm th}$ listed in Table I. Details of the determination of η are given in the subsequent section.

The neutrons traverse construction material and air on their flight paths. Additionally, 3.3 cm of lead was placed in front of the most forward and backward detector during some runs at $E_p = 800$ MeV, in order to suppress excessive γ radiation. We corrected for the flux attenuation due to this absorber [26].

B. Neutron detector efficiency

The neutron detector efficiencies $\eta(E_n^{\rm th}, E_n)$ used herein are based on Monte Carlo calculations with the code of Cecil *et al.* [27] for the detector sizes, hydrogen to carbon (H/C) ratios and thresholds $E_n^{\rm th}$ listed in Table I. The data base of the code allows coverage of the energy range $E_n \leq 300$ MeV with a quoted uncertainty of 10%. This would in principle be adequate for all 256 MeV and the low energy part of the 800 MeV data. It was, however, shown by Byrd *et al.* [28] for our 30.5 cm diam × 20.3 cm liquid scintillators, that the code overestimates the efficiency for such large detectors by 10–20 % which is attributed to light attenuation effects. Similar issues are discussed elsewhere [29, 30]. These problems can be circumvented by renormalizing the Monte Carlo results to an accepted reference value, and we shall now outline our procedure.

For reference the reaction ^{7}Li$(p, n_{0-1})^7$Be(g.s.+0.43 MeV) to the only particle stable state in ^{7}Be was taken. This L=0 transition is characterized by a prominent peak at small angles that can be resolved from the continuum in neutron TOF experiments. Taddeucci *et al.* [31] have shown for the energy range $E_p = 80 - 795$ MeV, that the differential cross sections of the transition can be reproduced by a universal function $\sigma(q)$ of the transferred linear momentum q, viz.,

$$\sigma(q) = \sum_{j=1}^{9} a_{0j} J_0 \left(z_{0j} \frac{q}{q_{\rm lim}} \right), \qquad (1)$$

where the J_0 is the Bessel function of order zero, z_{0j} are the zeros of J_0, $J_0(z_{j0}) = 0$, and $q_{\rm lim}$=2.6 fm^{-1} denotes the momentum transfer limit. The numerical coefficients a_{0j} given in Ref. [31] were derived from the angle integrated cross sections for the reaction, which can be measured accurately with activation techniques [32, 33].

At 256 MeV we have applied Eq. (1) to deduce the efficiency for the detector placed at 7.5°, i.e., for q=0.46 fm^{-1}, from the number $N_{\rm Li}$ of neutrons detected in the TOF peak of the ^{7}Be(g.s.+0.43 MeV) reaction. This experimental value for η amounted to 72.7% of the calculated one. Under the assumption that the efficiencies given by the code [27] exhibit the correct dependence on detector sizes, thresholds $E_n^{\rm th}$ and neutron energies, we have therefore normalized all calculated values to this experimental result. Details of the normalization are given elsewhere [34].

TABLE II. Error estimates.

Source of error	E_p = 256 MeV (% FWHM)	E_p = 800 MeV (% FWHM)
Detector efficiency	10.6	20.0
Flux attenuation	10.0	10.0
Beam current	2.0	5.4
Target thickness	1.5	1.5
Solid angle	0.2–0.8	0.2–0.8

The code does not take into account pion production in the liquid scintillator material as a reaction channel that, at least for $E_n > 300$ MeV, may eventually lead to neutron detection. It is reported [29, 30, 35] that the code's application to such high neutron energies yields efficiencies that, depending strongly on $E_n^{\rm th}$, are constant or decrease slightly with increasing E_n, whereas experimental results show the opposite trend.

At $E_p = 800$ MeV, the ^{7}Li$(p, n_{0+1})^7$Be transition could no longer be used for normalization purposes, because even at 7.5° the momentum transfer is considerable (q=0.81 fm^{-1}) and the cross section $\sigma(q)$ is so low that the overall time resolution achieved (see Table I) was not sufficient to resolve the transition. It was therefore decided to set $\eta(E_n^{\rm th}, E_n > 300$ MeV) to a constant value η_0. The numerical values for η_0 listed in Table I were deduced by averaging the normalized Monte Carlo results over the neutron energy interval 280–300 MeV. In view of the experimental information on $\eta(E_n^{\rm th}, E_n > 300$ MeV) mentioned above, η_0 can be considered a lower limit with an estimated uncertainty of 20%.

In order to independently check these efficiencies we have deduced them from data [36] for ^{27}Al and $^{\rm nat}$Pb(p, xn) at $E_p = 800$ MeV, whose efficiencies were ultimately derived from a separate ^{7}Li(p, n_{0+1}) measurement at 0°. Though these data are intended to focus on the evaporation component and have low resolution and statistics at high neutron energies, they may nevertheless give an impression of the extent of uncertainty introduced by the choice of the detector efficiencies (Fig. 3). Note that the cross sections for the normalized efficiencies are generally higher than those from the separate experiment, which is consistent with the assumption that the calculations represent a lower limit.

The detector efficiencies turn out to contribute most to the systematic errors that are listed in Table II. These errors sum up to 15% for $E_p = 256$ MeV and 23% for $E_p = 800$ MeV. Compared to these numbers, the uncertainties of the dead time corrections are negligibly small. The uncertainties due to counting statistics vary strongly with detector position and neutron energy; to give an example, cross sections of 1 μb/MeV sr were obtained at $\Theta_{\rm lab} = 150°$ with typically 300 detected neutrons per MeV.

C. General features

The resulting energy spectra from the reaction of 256 and 800 MeV protons with $^{\rm nat}$Zr and $^{\rm nat}$Pb are shown

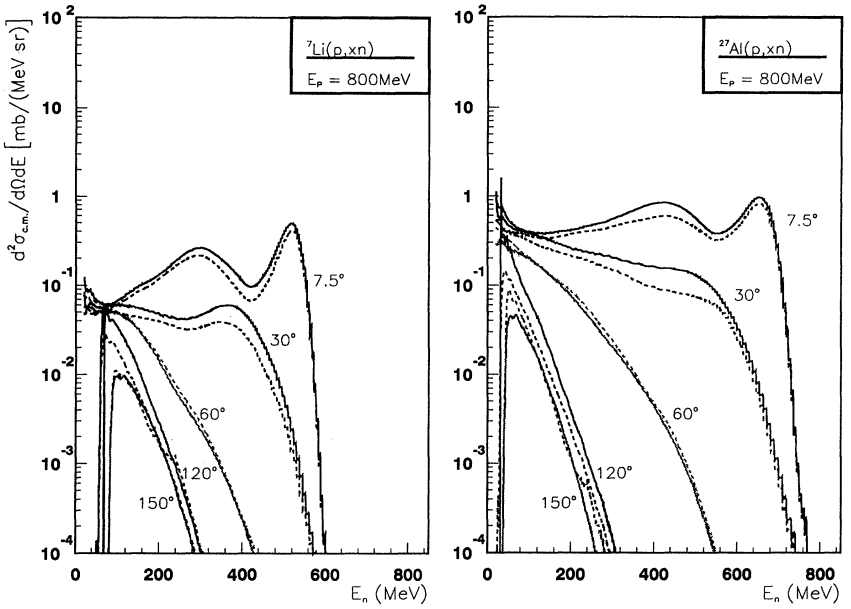

FIG. 3. Energy distributions for ^{7}Li(p,xn) and ^{27}Al(p,xn) reactions at 7.5° to 150°. For each angle spectra are shown calculated with the efficiency taken from [27] with a normalization by means of Eq. (1) (solid line), and an experimental efficiency (dashed line, see text).

in Figs. 4 and 5 along with calculations discussed in Sec. IV. They show little target specific features; the absolute cross sections for ^{7}Li, ^{27}Al, Zr, Pb(p,xn) scale as A^x with $x = 0.9 \pm 0.15$ for forward directions, which is in qualitative support of a nucleon-nucleon collision picture. All data, including those for ^{7}Li and ^{27}Al(p,xn) at 256 MeV which are not shown here, are available in tabular form [37].

In Fig. 6, we compare our 256 and 800 MeV ^{nat}Pb(p,xn) spectra with results from Ref. [25]. The agreement is quite satisfactory. Differences may be attributed to the detector efficiencies used, and at the highest energies the differences may be due to background subtraction techniques.

At 256 MeV, the spectra at 7.5° and 30° show flat continua resembling those of the (p,xn) data for $E_p \leq 160$ MeV [9]. The broad structure at 7.5° and residual excitation $E^* \leq 70$ MeV contains the unresolved contributions from the isobaric analog transition and the collective strength of the Gamow-Teller (L=0) resonance, the spin-flip dipole (L=1), and the quadrupole mode (L=2) resulting from direct one-step processes of one-particle–one-hole (1p-1h) spin-isospin excitation of the target nucleus [38]. At the backward angles $\Theta_{lab} = 120°$ and 150° the spectra exhibit almost exponential shapes. Their slopes, however, are not indicative of a thermal equilibrium, because they would correspond to nuclear temperatures of the order of 17 MeV. Moreover, the angular distributions do not, even for the lowest neutron energies $E_n = 30 - 50$ MeV, show indications for a component increasing beyond 90°. Therefore SMCE and even more equilibrium processes can certainly be excluded from discussion of the contributing mechanisms.

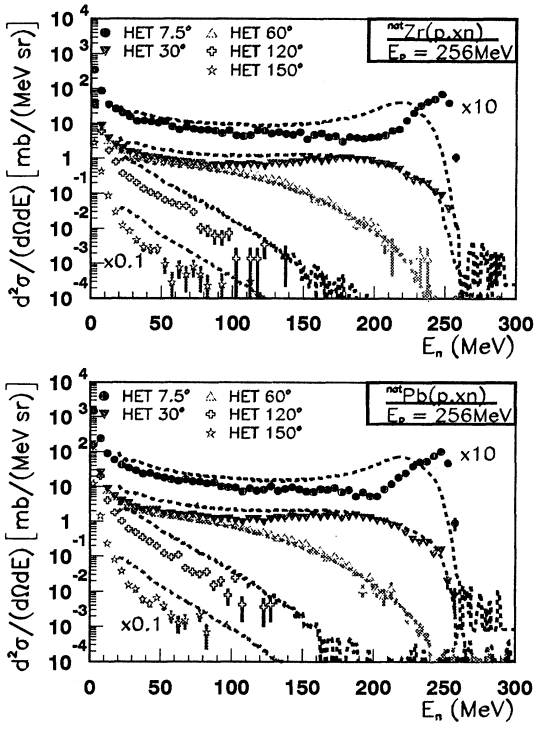

FIG. 4. Experimental (p,xn) spectra for ^{nat}Zr and ^{nat}Pb ırgets at $E_p = 256$ MeV. Experimental results are shown ɜ dashed lines. The points with error bars result from the ETC code; statistical uncertainties due to number of events ın for each point determine the error bar limits. The spectra t 7.5° (150°) have been shifted upwards (downwards) by one ecade.

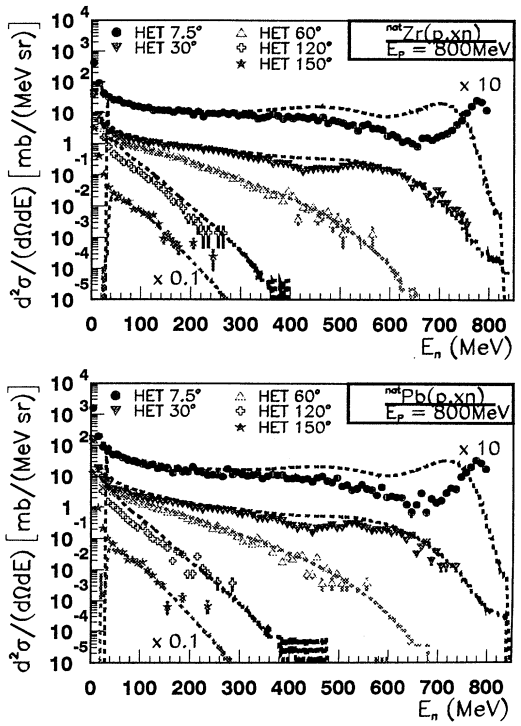

FIG. 5. As in Fig. 4, for 800 MeV incident energy.

Rather the spectra presented can provide information on intranuclear nucleon-nucleon collisions and thus on the strength of the effective nucleon-nucleon interaction.

These findings apply even more to the spectra obtained with 800 MeV projectiles which show an additional feature: At 7.5°, a broad peak is observed centered about 300 MeV below the ground state transition. This peak is attributed to neutrons following the quasifree pion production from reactions like $pn \rightarrow pn\pi^0, pn \rightarrow nn\pi^+$, and $pp \rightarrow np\pi^+$ [39], and its broadening is due to the momentum distribution of the nucleons in the nuclear environment and the pion momentum. Reaction models that do not include pionic degrees of freedom obviously cannot be expected to reproduce such a structure. This applies to the quantum statistical multistep as well as to the semiclassical preequilibrium models as presently formulated, whereas INC models generally do include these and other three-body channels.

IV. DISCUSSION

The subsequent discussion will focus on the Zr,Pb(p, xn) reactions, because (i) ^{7}Li is too light a nucleus for application of statistical models, and (ii) calculations for ^{27}Al yielded results in line with those for Zr and Pb, as was observed in [9], too.

A. Statistical multistep direct emission

In the FKK multistep model [5] a nuclear reaction is viewed as a sequential process chained by two-body interaction through states of increasing complexity. At each stage n, the theory considers two classes of reaction amplitudes: an SMCE (statistical multistep compound) contribution connecting only particle bound states (which can be neglected here) and the SMDE (statistical multistep direct) contribution. The latter proceeds exclusively through states with at least one nucleon being unbound; its contribution to the double different cross section can be calculated as [40, 41]

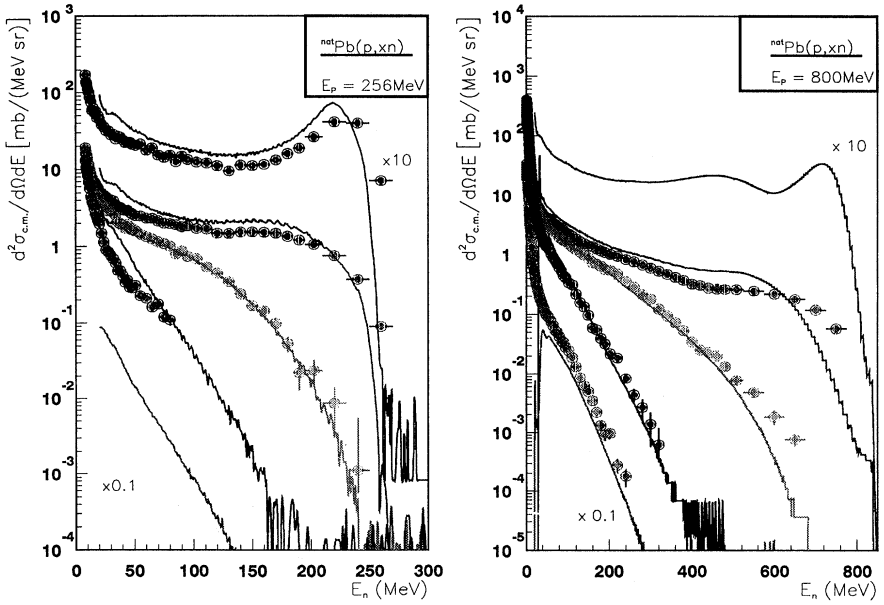

FIG. 6. Comparison of 256 and 800 MeV Pb(p, xn) data from this work with results of Ref. [25, 26]. The solid line gives results of the present work.

$$\frac{d^2\sigma}{dU\,d\Omega} = \sum_{n=2}^{n_{\max}} \sum_{m=n-1}^{n+1} \int \frac{d\mathbf{k}_1}{(2\pi)^3} \cdots \int \frac{d\mathbf{k}_n}{(2\pi)^3} \left[\frac{dW_{m,n}(\mathbf{k}_f, \mathbf{k}_n)}{dU_f d\Omega_f}\right] \cdots \left[\frac{dW_{2,1}(\mathbf{k}_2, \mathbf{k}_1)}{dU_2 d\Omega_2}\right] \frac{d^2\sigma_{1i}(\mathbf{k}_1, \mathbf{k}_i)}{dU_1 d\Omega_1}, \tag{2}$$

with the transition probability in the continuum region from the $(n-1)$th to the nth stage being given by

$$\frac{d^2W_{n,n-1}}{dU_n d\Omega_n} = 2\pi^2 \rho_c(\mathbf{k}_n)\rho_n(U_n)\langle|\nu_{n,n-1}(\mathbf{k}_n, \mathbf{k}_{n-1})|^2\rangle. \tag{3}$$

The $\mathbf{k}_i$, $\mathbf{k}_j$, and $\mathbf{k}_f$ denote the momenta of the initial, jth intermediate, and final step nucleon, respectively; m labels the exit mode. The quantity $\rho_c(\mathbf{k})$ gives the density of states for particles of momentum $\mathbf{k}$ in the continuum, and U_j is the excitation remaining in the residual nucleus after step j. The SMDE cross section is thus expressed as a convolution of $n_{\max}$ incoherent single-step contributions. The matrix element describes the transition from the $(n-1)$th to the nth stage; it is evaluated in Born approximation with optical model (OM) generated distorted waves χ:

$$\nu_{a,b}(\mathbf{k}_i, \mathbf{k}_f) = \int \chi_a^{(-)*}\langle\Psi_f|V(r)|\Psi_i\rangle\chi_b^{(+)}d\mathbf{r}. \tag{4}$$

The transition between the nuclear states Ψ_i and Ψ_f is mediated by the effective nucleon-nucleon interaction $V(r)$. The entrance step in Eq. (2) is composed of an energy average over the density $\rho_2(U)$ of 1p-1h states in the nucleus after the first collision of the incident proton, the corresponding spin distribution function $R_2(L)$, and the DWBA cross section for each of the orbital momenta L involved:

$$\frac{d^2\sigma_{1i}}{dU_1 d\Omega_1} = \sum_L (2L+1)R_2(L)\rho_2(U)\left\langle\frac{d\sigma_L^{(\mathrm{DW})}}{d\Omega}\right\rangle. \tag{5}$$

The single-step contribution is also added to the SMDE cross section of Eq. (2) in order to obtain the full direct cross section. All (partial) level densities ρ have been calculated with the equidistant Fermi gas model with Pauli corrections and a level density parameter $a = A/8.5$ MeV^{-1}; this implies the assumption of spectroscopic factors being equal to 1. All distorted wave functions were generated using the nucleon optical model potential of Ref. [42]. The bound and quasibound single particle and/or single hole states of excitation energies up to 100 MeV for evaluation of the DWBA matrix elements are based on the shell model of a spherical Nilsson potential and comply with energy and orbital angular momentum conservation. Further details are given in Refs. [9, 40].

For the residual interaction $V(r)$, a finite-range Yukawa potential with a range parameter $r_0 = 1$ fm has been chosen; its strength was initially set to the value $V_0 = 26 \pm 1$ MeV deduced [43] for (p,n) reactions with $E_p \leq 25$ MeV. Recent investigations of (p,n) experiments [8, 9] with projectile energies $E_p = 80 - 160$ MeV led to angular and spectral distributions that were in conflict with this value and required a monotonic decrease of V_0 with increasing E_p. The same observation was reported for (p,p') reactions on several targets in the energy range $E_p = 80 - 120$ MeV [10, 11]. To further investigate this trend, we applied the SMDE model to the 256 MeV (p,xn) data, keeping all parameters except V_0 fixed. The calculation extended up to $n_{\max} = 6$. With the contribution of the nth step being proportional to V_0^{2n}, the absolute values of the calculated cross sections are sensitive enough to V_0 to derive a best value by comparison with the experimental result to within $\Delta V_0 = \pm 1.5$ MeV including the experimental uncertainties quoted before.

The contributions of subsequent SMDE steps vary with ejectile energy E_n and angle Θ_{lab}. Figure 7 shows that the first two steps prevail only for high values E_n and forward angles $\Theta_{\mathrm{lab}} \leq 30°$, whereas higher order steps fall off by more than one order of magnitude. With increasing Θ_{lab} and decreasing E_n, higher order steps become more significant and eventually determine the shape of the angular distributions at backward angles. In particular, in the angular range $45° \leq \Theta_{\mathrm{lab}} \leq 90°$ where the angular distributions exhibit the steepest descent, the first step is *no longer* the dominant one.

The absolute cross sections, rather than the shapes

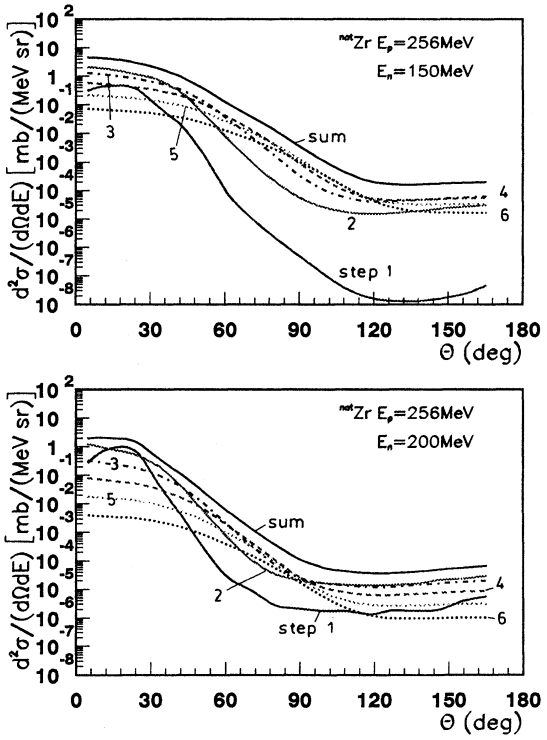

FIG. 7. Contributions of six steps of MSD reactions from FKK theory to the (p,xn) angular distribution of 256 MeV protons on $^{\mathrm{nat}}$Zr. The neutron energy is 150 MeV (upper) and 200 MeV (lower).

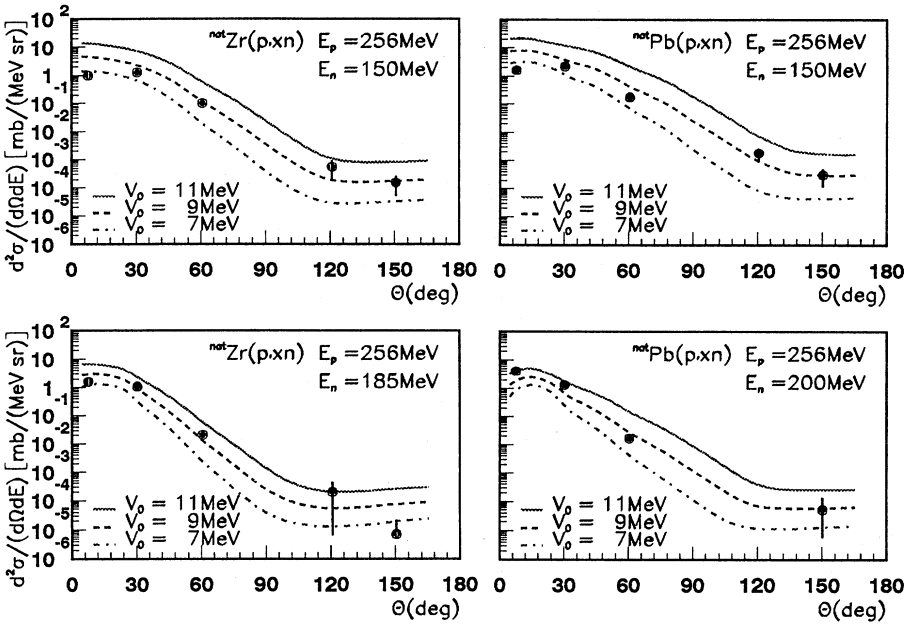

FIG. 8. FKK theory angular distributions for 256 MeV protons on ^{nat}Zr and ^{nat}Pb targets for ejectile energies of 150, 185, and 200 MeV. FKK results are shown for N-N potential depths of 7 to 11 MeV in 2 MeV steps.

of the angular distributions, allow us to determine V_0. Figure 8 demonstrates, for 4 representative cases, that $V_0 = 8.5$ MeV yields the best overall agreement and $\Delta V_0 = \pm 1.5$ MeV about mark the upper and lower limit of this normalization. There is certainly no agreement obtainable for $V_0 = 12.5$ MeV, which was the value found [9] for $E_p = 160$ MeV.

Figure 9 represents the energy dependence $V_0(E_p)$ deduced from the FKK analyses of previous (p, xn) and (p, xp) measurements [9,11,12,43], together with the present result for $E_p = 256$ MeV. It can be seen that the monotonic decrease of V_0 with increasing E_p continues, qualitatively reflecting the same trend in the central part of the spin-isospin independent effective nucleon-nucleon interaction. It was argued in Ref. [11] that this trend is comparable to the energy dependence of the real optical potential, as the latter depends on the strength of the effective N-N interaction. This energy dependence, however, has to be corrected for the gradual energy loss of the incoming nucleon in subsequent intranuclear interactions. Instead of folding a strength $V_0(E_p)$ into the FKK calculation [44] we assume here that emission from the first and second step are equally likely and normalize it to the DWBA value of V_0 at $E_p = 20$ MeV [11,43]. Applying this approximation to the optical potential found by Johnson *et al.* [45] for n+Pb, one obtains (with all energies in MeV)

$$V_0(E_p) \approx 30.8 \exp(-0.162E/30.8), \quad (6)$$

which is in excellent agreement with our experimental result, shown in Fig. 9.

B. Intranuclear cascade calculation

The INC code used was taken from the Jülich version of the HETC transport code [16]. It is essentially the model due to Bertini [1] when used to calculate thin target yields. In this formulation the nucleus is divided into three density regions corresponding to 90%, 20%, and 1% of the central nuclear density. Nucleon momenta for the ground state nuclei are given a Fermi momentum distribution in a local density approximation. Binding energies of all nucleons are assumed to equal that of the least tightly bound nucleon. Calculations of the fast cascade are terminated when nucleons are unbound by half the Coulomb potential at the nuclear surfaces; the residual nuclei are then treated by compound nucleus decay formulas, without an intermediate precompound decay

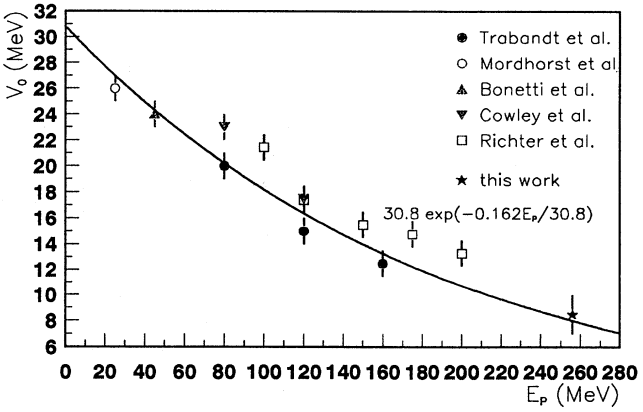

FIG. 9. Variation of the N-N potential depth V_0 as a deduced FKK fit parameter for (p, xn) and (p, xp) reactions from 25 to 256 MeV. Results are of this work and from Ref. [43] (open dot), [40] (triangle), [9] (solid dots), [12] (open squares), and [11] (inverted triangles). The solid line is the result of Eq. (6).

stage. Nucleon-nucleon collisions are followed as two-body processes in the mean potentials determined by the local densities. No reflection or refraction processes are considered. Above the pion threshold, the elastic two-body cross sections and kinematics are modified to include inelastic pion production processes; these rapidly become large with respect to elastic N-N scattering cross sections as energies exceed the pion thresholds [46].

Comparisons of the HETC INC code results with energy distributions for Zr and Pb targets at 256 and 800 MeV are shown in Figs. 4 and 5. In these figures the INC results are indicated by symbols with "error bars" representing the statistical uncertainties from the number of events in the Monte Carlo sampling. The experimental results are represented by dotted or dashed lines.

At all angles the spectral shapes for the 256 MeV data (Fig. 4) are represented quite well, except that the quasielastic peak at 7.5° is—as generally is the case for INC at very forward angles—overestimated. The absolute magnitude of calculated spectra 60° and forward is also in excellent agreement with data, with the exception of the quasielastic peak. As is common in the INC, the spectra at angles greater than 90° are underestimated. This discrepancy has been decreased in some codes by the inclusion of a precompound decay option prior to the equilibrium calculation [47].

The INC calculation presents an equally good interpretation of the 800 MeV data (Fig. 5). At 7.5°, the quasielastic peak is again overestimated and its broadening due to collective effects is missing. In contrast, the broad bump due to pion production in nucleon-nucleon collisions is underestimated at 7.5°, although it is prominent in calculations for $\Theta_{\rm lab} = 0°$. The yields at angles beyond 90° are improved versus data when compared with results at 256 MeV. In the following subsection, the crucial importance of explicit consideration of pion production at energies above 260 MeV will be seen. This is included in the INC model, and is inconsistent with the implicit assumptions of precompound decay models as presently formulated.

C. Precompound decay

Precompound decay models substitute partial state densities (exciton densities) for the partitioning of energy in successive two-body (nucleon-nucleon) scattering processes in the nucleus, with the assumption that every (energy conserving) partition for a given particle-hole number occurs with equal *a priori* probability [4]. This has been shown to be a reasonable result following from the kinematics of elastic nucleon-nucleon scattering processes for the first, i.e., three exciton configuration [48], but not for higher order terms [49]. Precompound models nonetheless have worked well, probably due to the dominance of the first collision term.

The angular distribution (or energy distribution at fixed angle) may be generated by a kernel based on the angular distribution of scattering of an incident nucleon from nucleons having a Fermi gas momentum distribution [50–52]. This result may be folded for higher order scattering, i.e., N-N scattering after the first event. These calculations are sometimes combined with additional folding to approximate "refractive" processes on entering and leaving the nuclear potential. The kinematic equations used are discussed in detail elsewhere [51, 52]. For comparison, we present here results calculated using only elastic N-N scattering kinematics, without "refractive" folding. At the energies of interest here, refractive corrections are in any case small.

In Fig. 10 we compare the experimental energy distributions for 256 MeV incident energy at the five angles of our experiment with results from the hybrid precompound plus Weisskopf-Ewing compound nucleus models from the ALICE code [17, 52]. The ALICE code used for these calculations was modified to use relativistic kine-

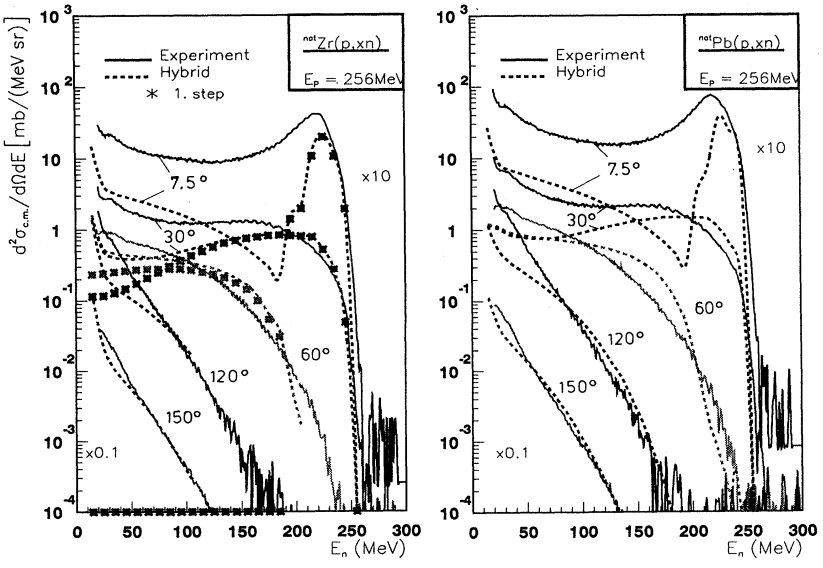

FIG. 10. Experimental 256 MeV (p, xn) spectra versus results calculated with the hybrid model (dashed). For interest, the contribution of the first N-N scattering term only is shown (as points) for the forward angles for the Zr target.

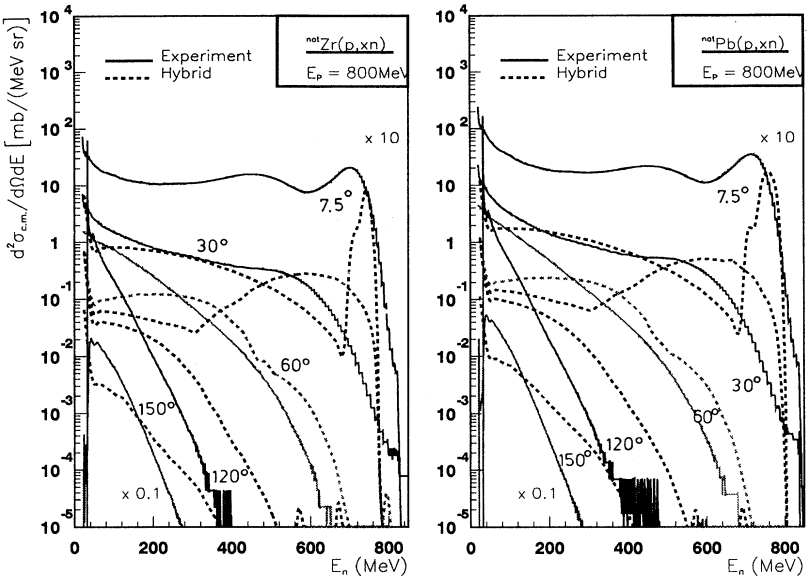

FIG. 11. As in Fig. 10 for 800 MeV incident energy.

matics for calculating single particle phase space factors and nucleon velocities.

The N-N scattering kernel used in conjunction with the hybrid precompound model gives reasonable spectral results for angles of 30° to 150°. The 7.5° result is very poor, showing the difficulty of reproducing the quasielastic scattering at very forward angles. The INC shares this difficulty, as it should, since both approaches are basically using the same scattering kinematics. The precompound calculation nonetheless gives poorer results than the INC at 7.5° for energies below the quasielastic peak; the reasons for this are not clear.

The precompound calculation gives somewhat better agreement with data at 120° and 150° than the INC; again the reasons are not clear. This regime consists of second and higher order scattering contributions, as the first collision cannot—in the absence of reflection and refraction—give nucleons beyond 90°. The back angle yields have generally been underestimated in semiclassical scattering models, as with the INC results here in Figs. 4 and 5. The INC overall gives better spectral shapes and angular distributions than the precompound model.

In Fig. 10 we also show the result of the first collision term to the calculated spectra. At 7.5° the quasielastic peak is solely due to the first collision; at energies below $\approx$ 180 MeV the energy distribution comes from second and higher order scattering events. The first scattering contributes more at 30° and 60°, and nothing—in a semiclassical calculation—beyond 90°.

In Fig. 11 we compare the hybrid precompound model energy distributions with experimental results for 800 MeV incident protons. Such a comparison should fail miserably—and does. This follows from the fact that the N-N pion channel, which is significantly larger than the elastic N-N cross section above the pion threshold [46], is not presently included in precompound decay modeling. The use of exciton densities is totally inappropriate in this regime. We would have first to derive densities that took cognizance of the dominant three-body (or two-body including delta) nature of the N-N scattering final state. The three-body effects are treated in the INC approach (actually as a delta plus nucleon final state), and the importance is clearly seen in comparing precompound model (Fig. 10) and INC model (Figs. 4 and 5) results.

V. CONCLUSIONS

We have presented energy distributions for (p, xn) reactions on ^{nat}Zr and ^{nat}Pb targets for incident energies of 256 and 800 MeV. Earlier measurements on ^{90}Zr and ^{208}Pb had been reported at energies of 25, 80, 120, and 160 MeV [8, 9, 43], and at 25, 35, and 45 MeV [53, 54]. Measurements in this work were made at angles of 7.5°, 30°, 60°, 120°, and 150°. Analyses via the FKK semidirect reaction theory required a depth V_0 of 8.5±1.5 MeV at E_p = 256 MeV for the N-N potential, consistent with the monotonic decrease with increasing energy deduced in earlier work.

The INC model of Bertini gave quite satisfactory spectral predictions for both targets, with some underestimation of magnitude at 120° and 150°. The precompound hybrid model, as implemented in the ALICE code, was less satisfactory than the INC at 256 MeV, and totally failed at 800 MeV. The latter result was expected due to the importance of three-body pion producing final states in nature, overwhelming the assumed two-body elastic N-N channels implicit in precompound decay models.

ACKNOWLEDGMENTS

We wish to express our appreciation to the WNR operations staff and Dr. D.A. Clark for cooperation that made this work possible. We appreciate the work of

Dr. J. Gilmore in providing the beam current normalizations using activation methods. The help of J. King was indispensable to this project. Finally the help and cooperation of Dr. P. Lisowski made this work possible and is greatly appreciated. This work was supported by the BMFT under Contract No. 06 HH 142 and by DOE under Contracts No. W-7405-ENG-36 and No. W-7405-ENG-48.

[1] H.W. Bertini, Phys. Rev. **188**, 1711 (1969).
[2] K. Chen, Z. Fraenkel, G. Friedlander, J.R. Grover, J.V. Miller, and Y. Shimamoto, Phys. Rev. **166**, 949 (1968).
[3] M. Blann, Phys. Rev. Lett. **27**, 337 (1971).
[4] M. Blann, Annu. Rev. Nucl. Sci. **25**, 123 (1975).
[5] H. Feshbach, A. Kerman, and S. Koonin, Ann. Phys. (N.Y.) **125**, 429 (1980).
[6] T. Tamura, T. Udagawa, and H. Lenske, Phys. Rev. C **26**, 379 (1982).
[7] H. Nishioka, J.J.M. Verbaarschot, H.A. Weidenmüller, and S. Yoshida, Ann. Phys. (N.Y.) **172**, 67 (1986); H. Nishioka, H.A. Weidenmüller, and S. Yoshida, *ibid.* **183**, 166 (1988).
[8] M. Trabandt, W. Scobel, M. Blann, B.A. Pohl, R.C. Byrd, C.C. Foster, S.M. Grimes, and R. Bonetti, Phys. Rev. C **39**, 452 (1989).
[9] W. Scobel, M. Trabandt, M. Blann, B.A. Pohl, B.R. Remington, R.C. Byrd, C.C. Foster, R. Bonetti, C. Chiesa, and S.M. Grimes, Phys. Rev. C **41**, 2010 (1990).
[10] S.V. Förtsch, A.A. Cowley, J.J. Lawrie, D.M. Whittal, J.V. Pilcher, and F.D. Smit, Phys. Rev. C **43**, 691 (1991).
[11] A.A. Cowley, A. van Kent, J.J. Lawrie, S.V. Förtsch, D.M. Whittal, J.V. Pilcher, F.D. Smit, W.A. Richter, R. Lindsay, I.J. van Heerden, R. Bonetti, and P.E. Hodgson, Phys. Rev. C **43**, 678 (1991).
[12] W.A. Richter, A.A. Cowley, R. Lindsay, J.J. Lawrie, S.V. Förtsch, J.V. Pilcher, R. Bonetti, and P.E. Hodgson, Phys. Rev. C **46**, 1030 (1992).
[13] W.G. Love and M.A. Franey, Phys. Rev. C **24**, 1073 (1981).
[14] M.M. Meier, D.B. Holtkamp, G.I. Morgan, H. Robinson, G.J. Russell, E.R. Whitaker, W. Amian, and N. Paul, Radiat. Eff. **96**, 73 (1986).
[15] S. Cierjacks, Y. Hino, F. Raupp, L. Buth, D. Filges, P. Cloth, and T.W. Armstrong, Phys. Rev. C **36**, 1976 (1987).
[16] P. Cloth, D. Filges, R.D. Neef, G. Sterzenbach, C. Reul, T.W. Armstrong, B.L. Colborn, B. Anders, and H. Brückmann, KFA Jülich Report Jüe-2208, 1988; K.C. Chandler and T.W. Armstrong, ORNL Report ORNL-4744; Nucl. Sci. Eng. **49**, 110 (1972).
[17] M. Blann, LLNL Laboratory Report JC109052, 1991 (unpublished); no report exists on the modifications described herein to relativistic kinematic and phase space calculation.
[18] W.B. Amian *et al.*, in *Proceedings of the International Conference on Nuclear Data for Science and Technology*, Fülich, 1991, edited by S.M. Qaim (Springer, Berlin, 1992), p. 696.
[19] P. Plischke, W. Scobel, and M. Bormann, Z. Phys. A **281**, 245 (1977).
[20] J.S. Gilmore, G.J. Russel, H. Robinson, and R.E. Prael, Nucl. Sci. Eng. **99**, 41 (1988).
[21] J.B. Cummings, V. Agoritsas, and R. Witkoves, Nucl. Instrum. Methods **180**, 37 (1981).
[22] J.D. Anderson, V.R. Brown, R.W. Bauer, B.A. Pohl, C.H. Poppe, S. Stamer, E. Mordhorst, W. Scobel, S.M. Grimes, and V.A. Madsen, Phys. Rev. C **41**, 1993 (1990).
[23] K. Knoche, L. Sprute, W. Behrmann, E. Mordhorst, W. Scobel, M. Strecker, B. Cramer, B. Gebauer, D. Hilscher, U. Jahnke, and E. Schwinn, Z. Phys. A **342**, 319 (1992).
[24] R. Madey, F.M. Waterman, A.R. Baldwin, J.N. Knudson, J.D. Carlson, and J. Rapaport, Nucl. Instrum. Methods **151**, 445 (1978).
[25] M.M. Meier, C.A. Goulding, G.L. Morgan, and J. Ullmann, Nucl. Sci. Eng. **104**, 339 (1990); **110**, 289 (1992).
[26] T.N. Taddeucci, code ATTENE, private communication.
[27] R.A. Cecil, B.D. Anderson, and R. Madey, Nucl. Instrum. Methods **161**, 439 (1979).
[28] R.C. Byrd and W.C. Sailor, Nucl. Instrum. Methods **A274**, 494 (1989).
[29] W.B. Amian, M.M. Meier, R.C. Byrd, C.A. Goulding, G.I. Morgan, and C.E. Moss, Nucl. Instrum. Methods **A313**, 452 (1991).
[30] S.D. Howe, P.W. Lisowski, G.J. Russell, N.S.P. King, and H.J. Donnert, Nucl. Instrum. Methods **227**, 565 (1984).
[31] T.N. Taddeucci, W.P. Alford, M. Barlett, R.C. Byrd, T.A. Carey, D.E. Ciskowski, C.C. Foster, C. Gaarde, C.D. Goodman, C.A. Goulding, E. Gülmiz, W. Huang, D.J. Horen, J. Larsen, D. Marchlenski, J.B. McClelland, D. Pout, J. Rapaport, L.J. Rybarcyk, W.C. Sailor, E. Sugarbaker, and C.A. Whitten, Jr., Phys. Rev. C **41**, 2548 (1990).
[32] J. D'Auria, M. Dombsky, L. Moritz, T. Ruth, G. Sheffer, T.E. Ward, C.C. Foster, J.W. Watson, B.D. Anderson, and J. Rapaport, Phys. Rev. C **30**, 1999 (1984).
[33] J.W. Watson, R. Pourang, R. Abegg, W.P. Alford, A. Celler, S. El-Kateb, D. Frekers, O. Häusser, R. Helmer, R. Henderson, K. Hicks, K.P. Jackson, R.G. Jeppesen, C.A. Miller, M. Vetterli, S. Yen, and C.D. Zafiratos, Phys. Rev. C **40**, 22 (1989).
[34] S. Stamer, W. Scobel, and R.C. Byrd, in Proceedings of Neutron Cross Section Standards for the Energy Region Above 20 MeV, edited by N. Olsson (OECD, 1991), Report NEANDC-305 'U', p. 154.
[35] S. Cierjacks, M.T. Swinhoe, L. Buth, S.D. Howe, F. Raupp, H. Schmitt, and L. Lehmann, Nucl. Instrum. Methods **192**, 407 (1982).
[36] W.B. Amian, R.C. Byrd, C.A. Goulding, M.M. Meier, G.L. Morgan, C.E. Moss, and D.A. Clark, Nucl. Sci. Eng. **112**, 78 (1992).
[37] W. Scobel, available on request.
[38] F. Osterfeld, D. Cha, and J. Speth, Phys. Rev. C **31**, 372 (1985).
[39] B.E. Bonner, J.E. Simmons, C.R. Newsom, P.J. Riley, G. Glass, J.C. Hiebert, Mahavir Jain, and L.C. Northcliffe, Phys. Rev. C **18**, 1418 (1978).
[40] R. Bonetti, M. Camnasio, L. Colli Milazzo, and P.E. Hodgson, Phys. Rev. C **24**, 71 (1981); (unpublished).
[41] H. Feshbach, Ann. Phys. (N.Y.) **159**, 150 (1985).

[42] D.G. Madland, in Proceedings of Preequilibrium Nuclear Reactions, edited by B. Strohmaier (OECD, 1988), Report NEANDC-245 'U', p. 103.
[43] E. Mordhorst, M. Trabandt, A. Kaminsky, H. Krause, W. Scobel, R. Bonetti, and F. Crespi, Phys. Rev. C **34**, 103 (1986).
[44] M.B. Chadwick, FKK code system SOPHOS, private communication; Report LA-UR-92-2346, 1992 (unpublished).
[45] C.H. Johnson, D.J. Horen, and C. Mahaux, Phys. Rev. C **36**, 2252 (1987).
[46] B.J. VerWest and R.A. Arndt, Phys. Rev. C **25**, 1979 (1982).
[47] R.E. Prael, Los Alamos National Laboratory Reports LA-UR-90-1620, 1990; LA-UR-89-3347, 1989 (unpublished).
[48] M. Blann and H.K. Vonach, Phys. Rev. C **28**, 1475 (1983).
[49] J. Bisplinghoff, Phys. Rev. C **33**, 1569 (1986).
[50] M.L. Goldberger, Phys. Rev. **74**, 1269 (1948).
[51] K. Kikuchi and M. Kawai, *Nuclear Matter and Nuclear Reactions* (North-Holland, Amsterdam, 1968).
[52] M. Blann, W. Scobel, and E. Plechaty, Phys. Rev. C **30**, 1493 (1984).
[53] W. Scobel, M. Blann, T.T. Komoto, M. Trabandt, S.M. Grimes, L.F. Hansen, C. Wong, and B.A. Pohl, Phys. Rev. C **30**, 1480 (1984).
[54] M. Blann, R.R. Doering, A. Galonsky, D.M. Patterson, and F. Serr, Nucl. Phys. **A257**, 15 (1976).